Physica Status Solidi B 2021, 258, 2000527

Study of Electronic States in $LaNiO_3/SrRuO_3$ Bilayers: Interface Induced Magnetism and Charge Transfer

R. G. Tanguturi [1], Peng Zhou[1], Zhuo Yan [1], Yajun Qi [1], Zhengcai Xia [2], Yong Liu [3], Rui Xiong [3], Yizhong Guo[4], Lihua Wang[4], G. Srinivasan[5], Tianjin Zhang [1]**

[1] Ministry of Education Key Laboratory for Green Preparation and Application of Functional Materials, Hubei Provincial Key Laboratory of Polymers, School of Materials Science and Engineering, Hubei University, Wuhan 430062, PR China

[2] Wuhan National High Magnetic Field Center, Huazhong University of Science and Technology, Wuhan 430071, People's Republic of China

[3] Department of Physics and Key Laboratory of Acoustic and Photonic Materials and Devices of Ministry of Education, Wuhan University, Wuhan 430072, China

[4]Institute of Microstructure and Properties of Advanced Materials, Beijing University of Technology, Beijing, 100022, P. R. China

[5] Physics Department, Oakland University, Rochester, MI 48309, USA

Abstract

We report results of a study on the electronic states and valence band offset in the heterostructures of the transition metal oxide $LaNiO_3$ (LNO)/$SrRuO_3$ (SRO) grown on (001) – $SrTiO_3$ (STO) substrates. X – ray photoelectron spectroscopy (XPS) data reveals the presence of Ni^{2+} states in LNO layer that could develop a reduced bandwidth of O 2*p* and Ni 3*d*. Further analysis of XPS data has confirmed that the presence of a valence band offset (VBO) and the value of VBO is found to be + 0.02 eV and – 0.38 eV for the bilayers of STO/$LaNiO_3$/$SrRuO_3$ (BL-1) and STO/$SrRuO_3$/$LaNiO_3$ (BL-2), respectively. The distinct signs of VBO have been noticed between the bilayers due to the relative shift of the valence band of the top layer with respect to the bottom layer. Such band shift can lead to the charge transfer across the (3d-4d) interface, which significantly modifies the global electronic transport and magnetic properties of bilayers. A detailed discussion on the underlying physical phenomena of electrical transport and magnetic responses triggered by the interface is also incorporated in this study.

Keywords: $LaNiO_3/SrRuO_3$ hetero-structure, interfacial charge transfer, valence band offset, electrical transport

*** Corresponding author:** *Yajun Qi (yjqi@hubu.edu.cn), Tianjin Zhang (zhangtj@hubu.edu.cn)*

I. Introduction

Perovskite oxides are promising materials for investigations on their functionalities towards new technological applications [1]. An immense variety of properties such as high mobility of electron gas, ferromagnetism, and interface induced superconductivity etc. have been explored in hetero-structures of perovskite oxide due to the deviation of ordering parameters at their interfaces [2, 3]. These new properties are generated by the reconstruction of electronic structures and manipulation of the degrees of freedom at/across the interface of multilayers.

The magnetic response at the interface of heterostructures originate from underlying magnetic phenomena such as anti-ferromagnetism, exchange bias, Dzyaloshinskii–Moryia coupling, Ruderman–Kittel–Kasuya–Yoshida (RKKY) interaction etc. [4, 5]. An interface induced antiferromagnetic (AFM) ordering is noticed in the heterostructures of $La_{0.7}Sr_{0.3}MnO_3$(LSMO)/$SrRuO_3$(SRO) whereas the constituent layers individually exhibit ferromagnetic ordering [6]. Such AFM ordering is further tuned while varying the thickness of any one of the ferromagnetic (FM) layers. For example, studies on the thickness dependence of magnetic interactions in $[\mathrm{LSMO}(t=20uc)/\mathrm{SRO}(n)]_{15}$ superlattices showed that the AFM interaction was weakened by increasing the thickness of the SRO layer [7]. Similar to many perovskite oxides, $LaNiO_3$ based multilayers significantly modifies their properties once the materials are transformed to heterostructures [8]. Superlattices of [$LaNiO_3$/$LaMnO_3$] grown along [111] orientation behaved like the ferromagnetic insulator double perovskite La_2MnNiO_6 [9-11]. Magnetic frustration and spin glass behaviour are other features observed in LNO based multilayers [12, 13]. In LSMO/LNO multilayers, oxygen vacancies, inter-diffusion of cation and/or charge across the interface, variation of the valence state etc. modified the spin ordering of LSMO layer such that the magnetic structure is accompanied by either a weak ferromagnetic or spin glass behavior [13].

Based on first principle calculations and transport properties, Qiao *et al* [14] demonstrated that the band structure of $LaNiO_3$ (LNO) thin films was transformed into a conducting metal from a semi-conducting behaviour when the ratio Ni^{3+}/Ni^{2+} ratio is increased. In addition, X-ray photoemission spectroscopy (XPS) results of Ni 3*p* core-level reported by Saghayezhian *et al.* supported the role of Ni^{3+}/Ni^{2+} ratio in restoring the metallic behaviour in LNO thin films by changing the film thickness [15]. Moreover, the presence of Ni^{2+} leads to the magnetic ordering observed in very thin films. Such states of Ni^{2+} may be present in a cluster of Ni^{3+} owing to the inevitable presence of oxygen vacancies in the LNO thin film. In recent reports [16, 17], ferromagnetic behaviour has been found in paramagnetic metallic LNO thin films with the polar metallic states where the states are controlled by the geometrically constrained substrates. Thus, the magnetic response of LNO triggered the electron transport between LNO and $SrIrO_3$ (SIO) layers to exhibit the low temperature metal to insulator transition in LNO/SIO heterostructure [18].

From all of the results from aforementioned studies, any change in the electronic structure in a heterostructure significantly amplifies the charge transfer across the interface and changes their magnetic properties. Though interface induced changes in physical properties have been reported for different combination of 3*d* and 4*d* transition metal oxide heterostructures, the underlying phenomena such as strain induced magnetism and modification of concentration of electronic states in the oxide heterostructure still need to be understood for engineered interfaces. Therefore, in this paper, we report the electrical and magnetic properties of $LaNiO_3/SrRuO_3$ bilayers on (001) STO substrate with altering stacks of depositions. In addition, the significant role of the interface in modifying the valence states and band structure of bilayers is also discussed in detail.

II. Experimental details

Thin films of $SrRuO_3$ (SRO) and $LaNiO_3$ (LNO) were grown on (100)-oriented $SrTiO_3$ (STO) substrates by PLD techniques. A KrF laser source (wavelength of ~ 248 nm) was used to create the ablation energy of 340 mJ with a repetition frequency of 2Hz. The deposition was carried out under the following conditions: substrate temperature of 700°C and oxygen partial pressure of 15 Pa. Subsequently, in-situ annealing process was carried out at the optimal deposition temperature of 700°C. The bilayers were deposited altering the layers arrangement with a fixed thickness i.e. STO/SRO (15 nm)/LNO (15 nm) and STO/LNO (15 nm)/SRO (15 nm); and the thickness SRO and LNO were 15 nm. The phase and purity of the grown hetero-structures was confirmed by X-ray diffractometer with Cu-Kα as the radiation source ($\lambda \sim 1.5405$ Å). Electrical transport behaviour was measured by using the physical property measurement system (PPMS - Quantum design) by the van der Pauw method. Temperature and field dependence of magnetic properties of the samples were investigated by using a superconducting quantum interference device (SQUID - quantum design) magnetometer. The element and valence states of the bilayers were measured by X-ray photoelectron spectroscopy

(XPS) with the source of Al K_α X-ray radiation of 1486.8 eV (Thermo Scientific Escalab 250 Xi with 150 W).

III. Results and Discussion

A. Structural characterisation

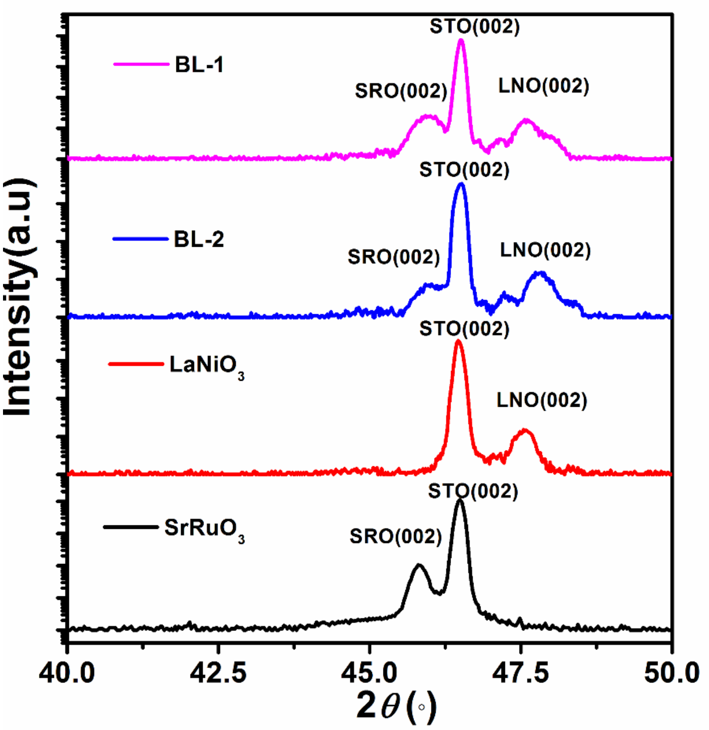

Fig.1: θ - 2θ scan of BL -1, BL – 2, and individual layers of LNO and SRO films around the (002) reflections.

Figure 1 shows X-ray patterns of STO/LNO/SRO (BL-1) and STO/SRO/LNO (BL-2) bilayers along with the individual layers of SRO and LNO on STO substrates. Out of plane lattice constants of BL-1 and BL-2 estimated from the reflections of (002) peaks were 3.817/3.945 Å and 3.941/3.802 Å, respectively. In the case of single layers, out of plane lattice constants of individual layer of $SrRuO_3$ and $LaNiO_3$ were 3.961 Å and 3.832 Å, respectively. The SRO film encountered an in-plane compressive strain whereas LNO film experienced a tensile strain by STO. With the introduction of an SRO layer between STO and LNO layers, the lattice constant of LNO layer abruptly dropped due to the lattice mismatch between SRO and LNO layers. However, the peak position of (002) for BL-2 bilayer was shifted to the higher angle side which suggests the tensile nature of LNO film grown on SRO layer increased due to the modifying octahedral structure of LNO layer. Similar to the case of BL-2, the BL-1 sample also exhibited a decrease in the lattice constant of the LNO layer, but the value was higher than that of BL - 2.

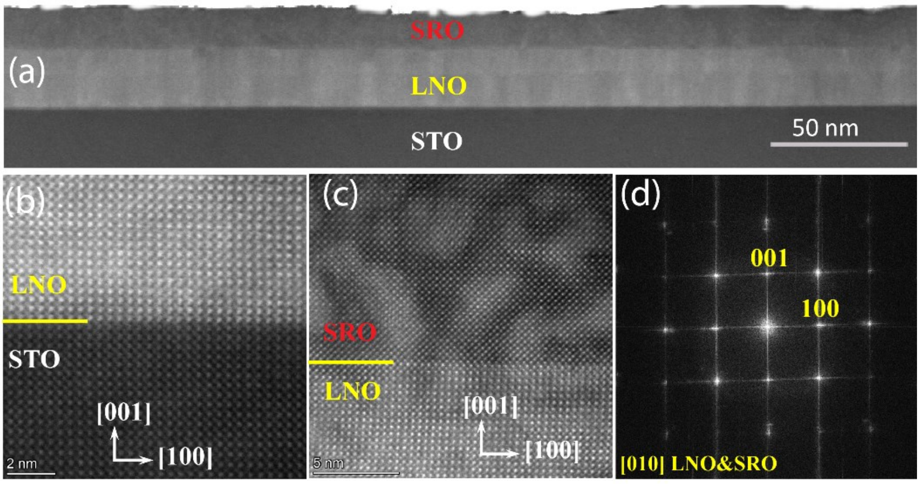

Fig. 2:Cross-sectional image of BL-1 bilayer films (*a*), high resolution TEM image of interface between STO/LNO (*b*) and LNO/SRO (*c*), and FFT patterns of LNO and SRO layers (*d*).

In order to confirm the quality of the interfaces and crystal arrangements of bilayer samples, we have recorded the cross-sectional transition electron microscopy (TEM) images of the BL-1 sample. Figure 2(*a*) depicts a clear interface between the two layers without any evidence for interatomic diffusion. Further, high resolution images of TEM are also shown in Figs.2 (*b*) and (*c*) for the respective interfaces of STO/LNO and LNO/SRO. These images provide further evidence for a clear atomically sharp interfaces with the epitaxial growth of films along the (001) orientation. Fast Fourier transformation (FFT) patterns (Fig.2 (*d*)) indicate that the epitaxial growth of the LNO/SRO films is in the (001) direction along with clear crystalline quality of the films.

B. XPS results

Figure 3 displays the XPS spectra of Sr 3*d* – core level, and Sr, Ru and O for the SRO layer as well as the BL-1 sample. The photoelectron spectrum of Sr was analyzed by considering the individual photoemission spectrum recorded for 3*d* – core level elements in the films. Here, the peak of Sr – 3*d* core level is split into a doublet of $3d_{5/2}$ and $3d_{3/2}$ positioned at 131 and 134 eV, respectively. These peaks originated from the spin orbit splitting with the energy separation of 1.8 eV [19]. In the present samples, the peak separation has been found to be 1.57 eV and 1.67 eV for SL – SRO and BL – 1, respectively. On one hand, the characteristic peaks of Ru-4*p*, Sr-4*s*, Sr-4*p*, O-2*p* and Ru-4*d* are found in the spectrum at 48, 37, 18, 8 and 1 eV, respectively. The peak of Sr-4*p* splits into the 3/2 and ½ due to the orbital distortion. The feature of Ru 4*d* resembles that of Ru^{4+} in the SRO layer which predominantly affects the metallic behavior of SRO [20]. Moreover, Ru^{4+} participated in the hybridisation with the O-2*p* to carry the charge transport via the Ru – O chain.

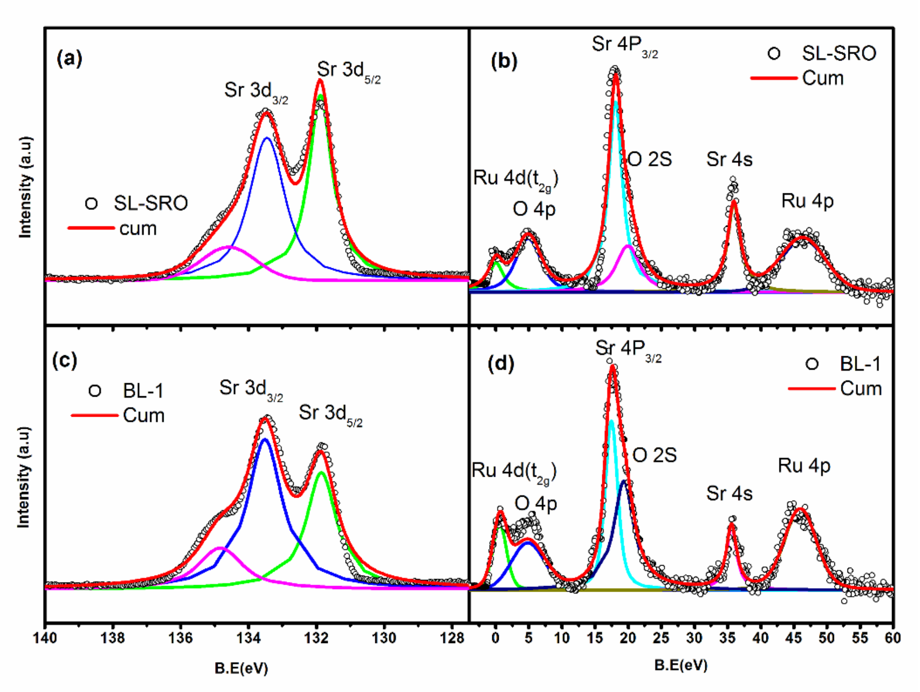

Fig.3: XPS spectra of Sr – 3*d* core level along with the fit of SRO film (*a*) and BL -1 (*c*). (*b*) and (*d*) are XPS data in the low binding energy region with core level ions of Sr, Ru and O elements of SRO and BL - 1 samples, respectively.

The core-level XPS of Ru - 3*p* orbital is shown in Fig.S1 (supplementary information) for both bilayers. The Ru - 3*p* orbital has a doublet of Ru - 3$p_{3/2}$ and Ru - 3$p_{1/2}$ peaks in both bilayers. This splitting comes from the spin - orbit splitting and the value of spin - orbit splitting is estimated to be 22.61 and 21.78 eV for BL -1 and BL -2, respectively. The full width at half maxima (FWHM) of Ru - 3$p_{3/2}$ is estimated to be 5.42, 5.88 and 4.23 for BL -1, BL -2 and SL - SRO samples, respectively. Such broadness of Ru 3$p_{3/2}$ implies that the Ru atoms in both bilayers have mixed oxidation states ranging from Ru^{4+} to Ru^{0+} [20].

On the other hand, the XPS spectrum recorded for the sample BL-2 is shown in Fig.4. The spectrum contains contributions from the core element of La 3*d* that is split into 3$d_{5/2}$ and 3$d_{3/2}$ with a separation of 16.8 eV. The satellite peak of La 3$d_{3/2}$ around 860 – 830 eV is associated with the valence states of Ni^{3+} and Ni^{2+} wherein the Ni features arise from the core level of 2$p_{3/2}$. The standard positions of Ni^{3+} and Ni^{2+} are at 856.3 and 852.2 eV, and they are located very close to La 3*d*3/2 core level. Therefore, it is difficult to analyze the profile of Ni $2p_{3/2}$ spectra due to the dominent La peak features. The intensity of the mixed state of La and Ni in bilayer samples is reduced due to variation of either Ni^{3+}/ Ni^{2+} ratio or the electronic state of Lanthanum. We analysed the lanthanum peak using peak fitting procedure. The binding energies of La doublet are 834.5 eV and 851.41 eV with the energy difference of 16.83 eV, but in the case of single LNO layer, the binding energies are 833.43 eV and 850.35 eV with the separation of 16.92 eV. Here, spin orbit splitting (SOS) of La $3d_{5/2}$ and La $3d_{3/2}$ core levels creates the separation of the peaks and the SOS value of bilayer sample (BL-2) is comparable to the previous reports [21]. Moreover, the obtained positions of Ni $2p_{3/2}$ are not accurate due to the domination of La contribution. In addition, the contribution of Ni $2p_{1/2}$ is noticed in the single LNO layer at around 873 eV and it is shifted in the bilayer. Such a feature indicates that the electronic states of Ni^{2+} are too sensitive to the strain induced by the buffer layer.

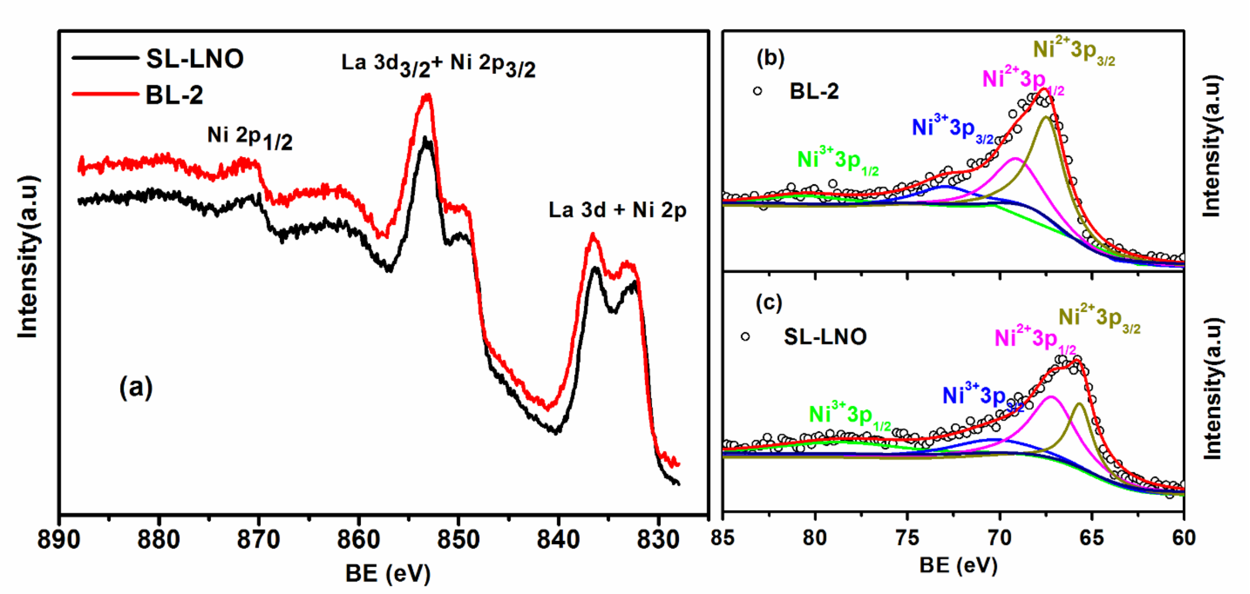

Fig.4: (*a*) XPS spectra of the $LaNiO_3$ and BL – 2 with the core level ions of La – 3*d* and Ni 2*p* orbitals. (*b*) & (*c*): Ni – 3*p* core level spectra of the LNO film and BL -2 along with the fit.

In order to overcome the complexity of mixed electronic states, the precise value of the Ni^{3+}/Ni^{2+} ratio is estimated through the Ni core level of $3p_{3/2}$ orbital. Though the relative intensity of Ni 3*p* is much lower than the intensity of Ni 2*p*, the Ni 3*p* is not associated with any other element. Thus the relative intensity ratio (RIR) is estimated by fitting Ni 3*p* peak and the fitting is shown in Figs.4 (*b*) and (*c*). The calculated values of Ni^{3+}/Ni^{2+} ratio are found to be 0.25 and 0.2 for single LNO and BL-2, respectively. Here, the value of RIR for single LNO is comparable to the theoretical value of spin – orbit splitting (SOS) [21]. Furthermore, presence of Ni^{2+} states in the single layer possesses a larger ionic radius than the Ni^{3+} and modifies the bond length of Ni – O. Moreover, the high value of RIR in the bilayer implies that the metallic behaviour of LNO might be influenced by the strain of Ni - O. Therefore, the overlap between the two bandwidths is reduced so that the metallic behaviour is weakened in LNO layer.

In addition to strengthening the analysis of the electronic structure, we have estimated the change in the valence states of the bilayers with the depth profiling measurement from the surface of bilayers towards the interior of the films. Here the Ar^+ etching process for both bilayers was done systematically for etching time from 0s to 75s. Figure 5 shows the plots of etching time versus energy difference (ΔE) of spin orbit splitting of Ru 3*p* peak of BL-1 and Ni^{3+}/Ni^{2+} ratio of Ni- 3*p* peak of BL-2. These values are calculated from the XPS spectra of Ru - 3*p* and Ni - 3*p* peaks for both bilayers. The fittings are shown in the supplementary Figure S3. Here Ni^{3+}/Ni^{2+} ratio of BL-1 sample and ΔE values of BL-2 are excluded from the graph due to the inaccuracy values of the intensity of signals from the bottom layer. The energy separation (ΔE) of Ru - 3*p* implies that there is a negligible change found in the valence states of BL-1 sample. However, the valence states ratio of Ni for BL-2 is decreased while increasing the etching time so that the development of Ni^{2+} states could be modified around the interface.

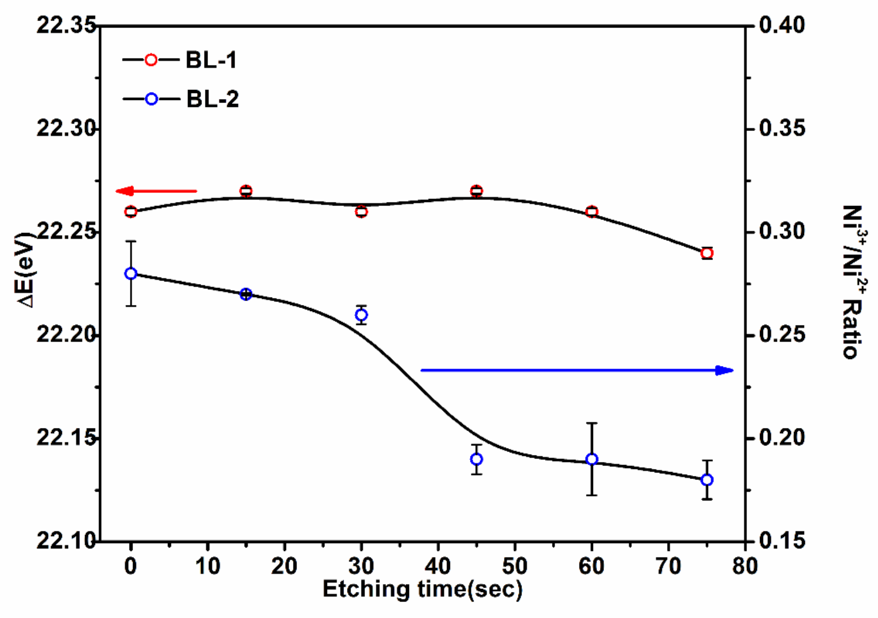

Fig. 5: Plots of etching time dependent spin orbit splitting energy and Ni^{3+}/Ni^{2+} ratio for BL-1, BL-2 samples.

For further understanding of the electronic structure of the bilayers, we iterated the band structure of the bilayers to find the valence band offset which yields an indispensable evidence for the functioning of the local oxide interface environment. The core level atoms in the bilayers and the valence band offset are estimated by the Kraut's equation [22, 23]

$$\Delta E_{\mathrm{VBO(A/B)}} = (E_{CL(A\text{-}I)} - E_{CL(B\text{-}I)}) - [(E_{CL(A)} - E_{V(A)}) - (E_{CL(B)} - E_{V(B)})] \quad (1)$$

Here ΔE corresponds to the VBO top layer relative to the bottom one. A and B represent the layer of SRO and LNO for BL-1 and in the case of BL-2 sample, the labels are interchangeable. The term $E_{CL(A\text{-}I)} - E_{CL(B\text{-}I)}$ is the energy difference between core level atoms of Ru - 3*p* and Ni - 3*p* in SRO/LNO heterostructures. $(E_{CL(A)} - E_{V(A)}) - (E_{CL(B)} - E_{V(B)})$ is the energy difference between core level and valence band maxima of top layer and bottom layer, respectively. The valence band maximum of the bilayers as well as the single layers is determined by extrapolating the linear part of the valence band spectrum edge to the baseline. These values are found to be –1.23 eV and –1.32 eV for SL-SRO and BL-1, – 0.78 eV and – 0.55 eV for SL – LNO and BL – 2, respectively. The corresponding values of VBO have been estimated as + 0.02 eV and – 0.38 eV for BL-1 and BL-2, respectively. These are comparable to the previous reports on LSMO/LNO and LMO/LNO hetero-structures [24]. The positive/negative sign of VBO signifies that the relative change of valence band of the top layer is either enhances or reduces the binding energy compared with the bottom layer.

C. Electronic transport properties

In order to understand the pivotal role played by the valence states on transport behaviour of SRO and LNO thin films, we measured the electronic transport behaviour as a function of temperature for the single layer and bilayers, and the curves are shown in Fig.6. BL -1 shows metal to insulator transition around 150 K that is the significant feature of SRO layer. However, the transition temperature of single SRO layer has been found at 160 K that is almost comparable with the previous reports [25]. On the other hand, electron transport response of single LNO layer and BL-2 exhibit metallic behaviour in the entire temperature scale. The magnitude of resistivity of the BL-1 sample is much higher than that of the single SRO layer, whereas, the values of resistivity of BL-2 samples drop to half the value for single layer LNO sample. Such overall enhanced conductivity in BL – 2 may cause transfer of the charge carriers across the interface.

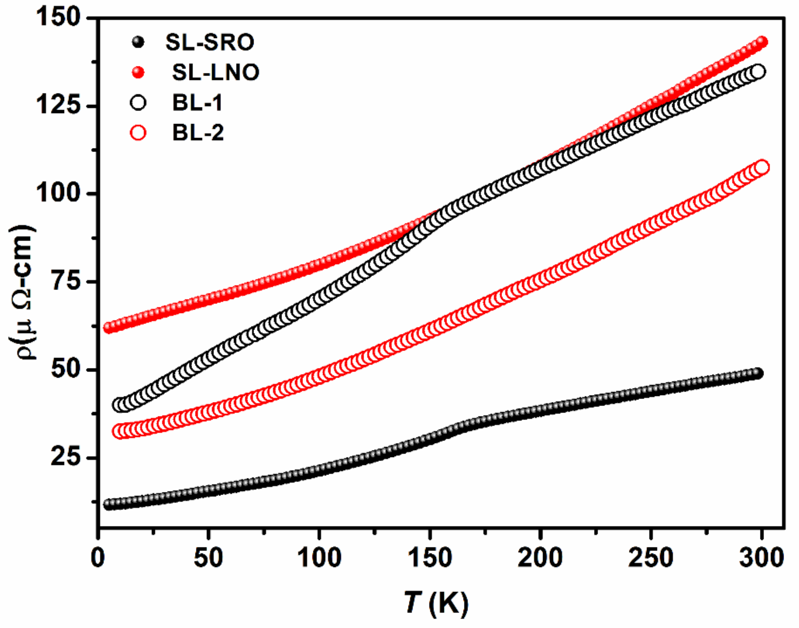

Fig.6: Temperature dependence of electrical resistivity for single layer and bilayer films.

The low temperature resistivity data of all the samples have been analysed by using the relation [26, 27]

$$\rho\ (T) = \ \rho_0 + \rho_1 T^n \qquad (2)$$

Here ρ_0 and ρ_1 are the residual resistivity, temperature dependent resistivity coefficient, respectively, and the value of n is in the range of 1 to 2 and the transport phenomenon originates from the interaction of different charge entities. Results of fitting the data to Eq. (2) wherein the exponent term is considered as free fitting parameter are shown in Fig.S3 (supplementary information). In particular, the resistivity data of sample BL-1 is fitted with $n = 1$, the value expected for electron – phonon scattering, whereas the exponent value is ~ 1.5 for the data of single layered SRO film. The $T^{1.5}$ dependence could be attributed to the combination of electron – phonon scattering (*EPS*) and electron – electron scattering (*EES*) mechanisms. On the other hand, the data for single layer LNO is well described by the $\rho\ (T)$ equation with the exponent of $n = 1$ but the values is around 1.5 for BL – 2 [27].

The electron – phonon constant (λ) could be estimated from the fitted values of resistivity curve for BL-1 by using the relation: $\lambda = 0.246\left(\hbar\omega_p\right)^2 \rho_1$[14]. Here $\hbar$ is a reduced Plank constant, ω_p is plasma frequency and $\rho_1$is fitting term of EPS. The plasma energy ($\hbar\omega_p$) of bilayer is calculated through Drude plasma frequency relation: i.e. $\left(\omega_p\right)^2 = (4/3)e^2 N_F (v_F)^2$, N_F and v_F are density of states and velocity of Fermi surface, respectively. By considering the values of charge concentration (n) and v_F are 1.2×10^{22} cm^{-3} and 2×10^{7} cm/s [28], the plasma energy and the value of λ for BL-1 are estimated to be 1.5 eV and 0.17, respectively. Similarly we have calculated the plasma energy and electron – phonon constant for single LNO film. The values of $\hbar\omega_p$ and λ are comparable to the values for BL -1 sample and to previously reported values for LNO thin films [29, 30]. Such a close value of SL - LNO and BL - 1 suggest that the valence bands of SRO layer might be modified by the buffer layer LNO.

Unlike the case for BL – 1, BL – 2 shows that the $T^{1.5}$ dependence could govern the localized spin fluctuations; with such contributions from Ni^{2+} ions [10]. A similar trend of $T^{1.5}$ dependent resistivity is often observed in $LaNiO_3$ due to the deficiency of oxygen induced Ni^{2+} states [30]. The coefficient of $T^{1.5}$ term correlates with the concentration of localized electrons in LNO in accordance with the ref [31], in which the coefficient is also associated with the magnetic terms such as spin - spin coupling constant (J) and spin (S) state. However, SRO films have non – Fermi liquid (NFL) behaviour over the temperature range 50 – 140 K which replicates the $T^{1.5}$ dependence. The coefficient of $T^{1.5}$ term is 2.52×10^{-2} μΩ - cm$^{1.5}$ and it is comparable to value of 2.98×10^{-2} μΩ - cm$^{1.5}$ for SRO thin films [32]. These parameter values are indicative of the underlying physical behaviour of both NFL and spin fluctuations.

D. Magnetic Properties

Figure 7(a) shows zero field cooled (ZFC) and field cooled (FC) magnetisation curves measured as a function of temperature when a magnetic field of 5kOe is applied along the plane of the films. Both bilayers exhibit ferromagnetic order at low temperatures. Magnetic transition temperature of bilayers is determined from the temperature derivative of magnetisation versus temperature curves and the transition temperature T_C are 148 K and 138 K for BL-1 and BL-2, respectively. In the case of single SRO layer, the magnetisation data are shown in Fig.S4 (Supplementary information). The T_C value of 140 K is comparable to the transition temperature of bilayers. Besides, there is another transition at 116 and 112 K for BL-1 and BL-2, respectively, which reveals the presence of spin glass behaviour in the present bilayer samples [33, 34]. The FC curves of both samples show a bifurcation while decreasing the temperature below T_C. The bifurcation of magnetisation curves suggests that the spin glass behaviour is present in both bilayers. Such a spin glass behaviour may originate from the finite size effect, slow domain growth and spin canting etc.[35, 36].

For further understanding of the spin glass behaviour, measurements on the temperature variation of the magnetisation were carried out in the presence of magnetic fields of 1kOe and 2kOe and the data are shown in Fig. 7(*c*) and (*d*). The blocking temperature gradually shifts towards the low temperature region which suggest that the spin glass behaviour could be due to the finite size effect.

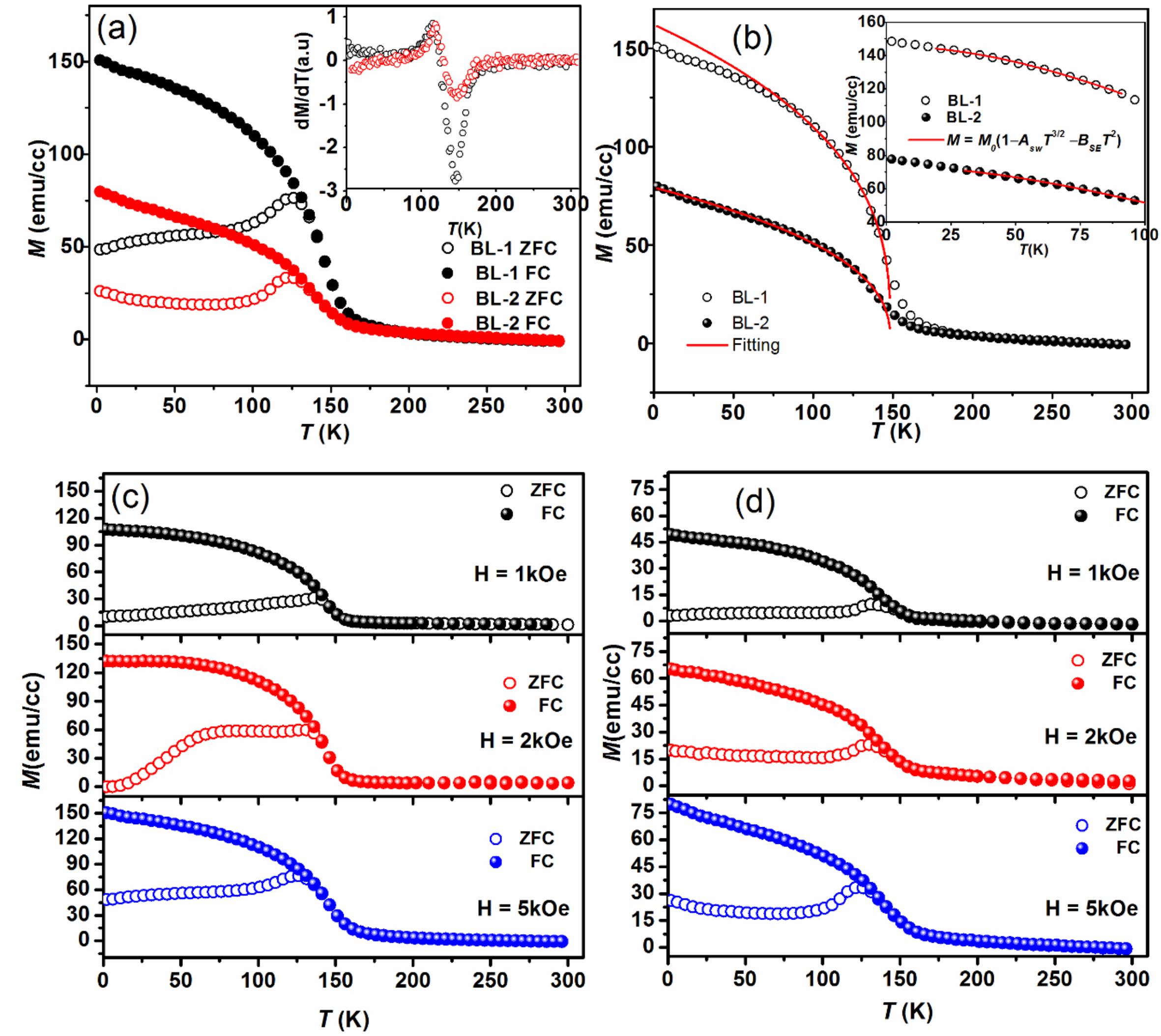

Fig.7: (*a*) Zero field cooled (ZFC) and field cooled (FC) magnetisation versus temperature data for the bilayers for a magnetic field of 5kOes along the plane of the films. The inset shows estimated d*M*/d*T* versus *T*. (*b*) The fit of FC curves to equation for the scaling theory and inset of represents the fit of magnetisation data to Eq. (3).

The magnetic response of both bilayers show a dissimilar trend in the ZFC curves with high magnetic moment for the BL-1 film than that of the BL-2 sample for decreasing temperatures. Such variation might be due to the presence of interfacial interaction between the SRO and LNO layers [37]. Otherwise, both bilayers are supposed to exhibit a unique magnetic behaviour like the SRO layer. Thus the magnetic interaction across the interface play a key role in modifying the magnetic moment of Ru in the bilayer samples. In order to understand the influence of the interface upon the magnetic moment of Ru, we employed the scaling theory, i.e. $M \propto (T_C - T)^{\beta}$, to analyse the spontaneous magnetization of bilayers around transition temperature [38]. From the fitting, the value of exponent has been found to be 0.34 and 0.39 for BL – 1 and BL–2, respectively. These values show that the magnetic interaction of BL – 1 sample is 3D – Ising type and in the case of BL – 2, the magnetic ordering is similar to the 3D – Heisenberg type ferro-magnets. On the other hand, in the case of itinerant ferromagnetic case, the presence of thermally excited magnons as well as Stoner excitations cause a reduction in the low temperature magnetization for increasing temperature. The FC data of bilayers are fitted to the relation:

$$M = M_0(1 - A_{sw}T^{3/2} - B_{SE}T^2) \tag{3}$$

Here $M_0$is magnetic moment at zero K, A_{sw} and B_{SE} represent the spin wave parameter and stoner excitation, respectively [39]. These constants are extracted from the fitting and is shown in the inset of Fig.7 (*b*). The values of A_{sw} have been found to be 2.31 × 10^{-4} and 2.88 × 10^{-4} for BL-1 and BL- 2, respectively. Here, the exchange interaction *J* between two Ru^{4+} ions is directly proportional to $A_{sw}^{-2/3}$ [40]. Thus, it is possible to extract the value of the exchange interaction between ions as well as interface charge transfer. The exchange term can be expressed in terms of spin (*S*) state and A_{sw} as: $A_{sw} = (0.0587/S)(k_B/JS)^{3/2}$. The values of *J* are estimated to be 40 k_B and 34 k_B for BL-1 and BL-2, respectively. These values are much higher than that of previous reports on SRO thin films [38]. The enhanced magnetic interaction constant suggests that the charge transport can take place across the interface.

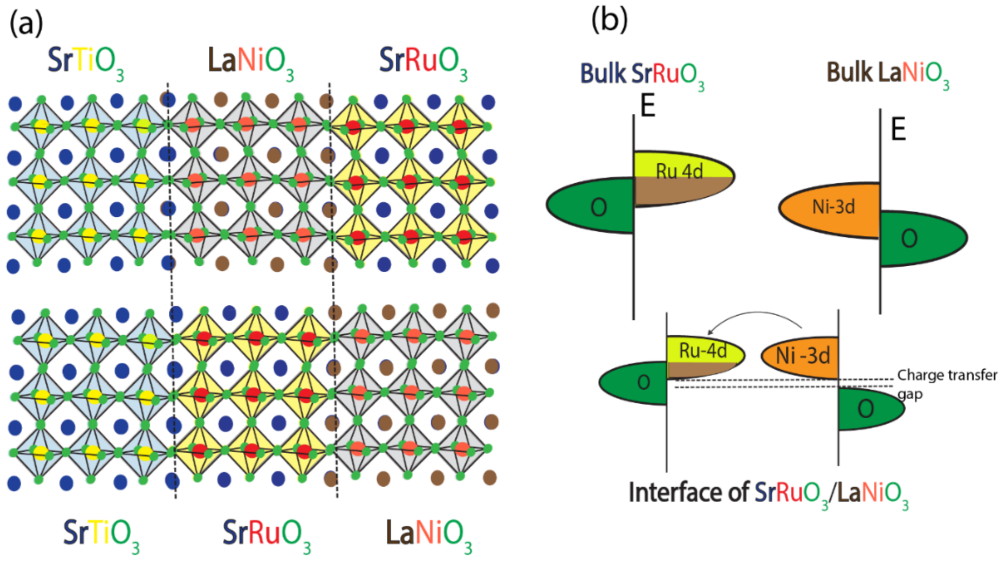

Fig. 8: (*a*) Schematic representation for the local environment of the interface for both bilayers. (*b*) Diagram showing the energy band of SRO/LNO interface along with the charge transfer direction and a charge transfer gap appears due to the presence of Ni^{2+} ions.

Figure 8(*a*) shows a schematic representation of the local environment in SRO/LNO bilayers. The sandwich layer in both bilayers is strongly influenced by the induced strain of substrate as well as top layer. Here it is worth to mention that an abrupt change in the out - of - plane lattice constants of LNO is due to the lattice strain in the LNO film. Moreover, the presence of Ni^{2+} states and the bond length of Ni - O further influence the nature of the octahedral of NiO_6. However, an equivalent value of out - of - plane lattice constants of SRO in bilayers may be due to the robust nature of RuO_6 octahedral than that of LNO. In the present bilayers, the overall magnetic and electrical responses are mainly dependent upon the redistribution of electronic states of Ni 3*d* and Ru 4*d* ions at the interface.

In general, the electron affinity of Ru^{4+} ions is lower than that of Ni^{3+} ions [41] so that the t_{2g} orbitals of Ru^{4+} ions are higher above those of Ni^{3+} ions. Moreover, at the interface, a strong hybridisation occurs to form a network of Ru 4*d* – O 2*p* – Ni 3*d*. The valence states of O - 2*p* at the interface need to adjust with the Fermi energy to get the equilibrium. Also, the presence of Ni^{2+} states implies that there is a chance of reduction in the degree of hybridization between the bands of Ni – O in the network. Further, the relative motion of VBO suggests that the e_g states of Ru^{4+} ions can modify to gain an electrons from either e_g state of Ni^{2+} or the t_{2g} states of Ru^{4+}. Subsequently, the oxygen between the two ions rearrange the states of e_g orbital of Ru with respect to e_g orbitals of Ni [42]. Such a band reconstruction at the interface is shown in Fig. 8(*b*). Here, two different colored regions of Ru 4*d* band refer to the electron occupying

t_{2g} states and empty e_g states. Thus the charge transfer is the likely cause of the estimated enhanced magnetic interaction terms in our calculations and RIR ratios of XPS results. Furthermore, other e_g orbitals of the neighbouring atoms of Ru initiate the double exchange interaction that implies the formation of spin pinning region at the interface [43]. Thus, it seems that the interfacial charge transfer of SRO/LNO can compete along with the bulk properties of the individual layers.

IV. Conclusions

We have presented evidence for the vital roles of the interfaces in determining the electrical and magnetic properties of LNO/SRO bilayer films with alternating stack arrangement. The out - of- plane lattice constant of LNO layer in both bilayers are strongly influenced by the strain, whereas the SRO layer has almost the same lattice constant value. XPS results have shown plausible evidence to the existence of Ni^{2+} states at the interface. These states can cause a charge transfer gap between the valence and conduction states. Moreover, the electronic transport behaviour of the bilayers has shown an apparent modified metallic behaviour. In addition, the bilayers show a distinct magnetic transition accompanied by a bifurcation in the magnetization versus temperature data that is indicative of enhancement in the effective magnetic interaction in the bilayers. Such enhancement in electrical and magnetic interactions of SRO/LNO bilayers might be due to the charge transfer across the interfaces.

Acknowledgements

RGT acknowledges China Postdoctoral Council for their financial assistance through International post–doc exchange program in 2018. RGT and YJQ are also grateful for the preliminary experimental support of PPMS facility at department of Physics, Zhengzhou University of Light Industry, Zhengzhou, China. YJQ acknowledges support from the Natural Science Foundation of China (11974104). Prof. Xia is thankful for the financial support of National Natural Science Foundation of China (Grant No. 11674115, 51861135104). This work also thanks the support from the Program of Introducing Talents of Discipline to Universities ("111 Project", D18025) China. LHW acknowledges support from the Beijing Outstanding Young Scientists Projects (BJJWZYJH01201910005018).

References

[1] J. Mannhart, D.G. Schlom, Science, **2010**, 327, 1607-1611.
[2] G. Zhou, F. Jiang, J. Zang, Z. Quan, X. Xu, ACS applied materials & interfaces, **2018**, 10, 1463-1467.

[3] A. Brinkman, M. Huijben, M. van Zalk, J. Huijben, U. Zeitler, J.C. Maan, W.G. van der Wiel, G. Rijnders, D.H. Blank, H. Hilgenkamp, Nature materials, **2007**, 6, 493-496.

[4] K.R. Nikolaev, A.Y. Dobin, I.N. Krivorotov, W.K. Cooley, A. Bhattacharya, A.L. Kobrinskii, L.I. Glazman, R.M. Wentzovitch, E.D. Dahlberg, A.M. Goldman, Physical review letters, **2000**, 85, 3728-3731.

[5] S. Das, S. Ghosh, P. Pramanik, D.C. Joshi, S. Thota, Journal of Physics D: Applied Physics, **2018,** 51, 325001.

[6] I. Lindfors-Vrejoiu, M. Ziese, physica status solidi (b), **2017**, 254, 1600556.

[7] P. Padhan, W. Prellier, R.C. Budhani, Antiferromagnetic coupling and enhanced magnetization in all-ferromagnetic superlattices, Applied Physics Letters, **2006**, 88, 192509.

[8] S. Middey, J. Chakhalian, P. Mahadevan, J.W. Freeland, A.J. Millis, D.D. Sarma, Annual Review of Materials Research, **2016**, 46, 305-334.

[9] H. Wei, J.L. Barzola-Quiquia, C. Yang, C. Patzig, T. Höche, P. Esquinazi, M. Grundmann, M. Lorenz, Applied Physics Letters, **2017**, 110, 102403.

[10] S.J. May, T.S. Santos, A. Bhattacharya, Physical Review B, **2009**, 79, 115127.

[11] J. Hoffman, I.C. Tung, B.B. Nelson-Cheeseman, M. Liu, J.W. Freeland, A. Bhattacharya, Physical Review B, **2013**, 88, 144411.

[12] G.-w. Zhou, X.-f. Guan, Y.-h. Bai, Z.-y. Quan, F.-x. Jiang, X.-h. Xu, Nanoscale Research Letters, **2017**, 12, 330.

[13] J.C. Rojas Sánchez, B. Nelson-Cheeseman, M. Granada, E. Arenholz, L.B. Steren, Physical Review B, **2012**, 85, 094427.

[14] L. Qiao, X. Bi, EPL (Europhysics Letters), **2011**, 93, 57002.

[15] M. Saghayezhian, Z. Wang, H. Guo, Y. Zhu, E.W. Plummer, J. Zhang, Physical Review B, **2017**, 95, 165434.

[16] T. Asaba, Z. Xiang, T.H. Kim, M.S. Rzchowski, C.B. Eom, L. Li, Physical Review B, **2018**, 98, 121105(R).

[17] T.H. Kim, D. Puggioni, Y. Yuan, L. Xie, H. Zhou, N. Campbell, P.J. Ryan, Y. Choi, J.W. Kim, J.R. Patzner, S. Ryu, J.P. Podkaminer, J. Irwin, Y. Ma, C.J. Fennie, M.S. Rzchowski, X.Q. Pan, V. Gopalan, J.M. Rondinelli, C.B. Eom, Nature, **2016**, 533, 68-72.

[18] Y. Li, J. Zhou, D. Wu, ACS applied materials & interfaces, **2019**, 11, 3565-3570.

[19] D.E. Barlaz, R.T. Haasch, E.G. Seebauer, Surface Science Spectra, **2017**, 24, 024002.

[20] M. Mlynarczyk, K. Szot, A. Petraru, U. Poppe, U. Breuer, R. Waser, K. Tomala, Journal of Applied Physics, **2007**, 101, 023701.

[21] S. Mickevičius, S. Grebinskij, V. Bondarenka, B. Vengalis, K. Šliužienė, B.A. Orlowski, V. Osinniy, W. Drube, Journal of Alloys and Compounds, **2006**, 423, 107-111.

[22] E.A. Kraut, R.W. Grant, J.R. Waldrop, S.P. Kowalczyk, Physical Review B, **1983**, 28, 1965-1977.

[23] S. Dewan, M. Tomar, A. Goyal, A.K. Kapoor, R.P. Tandon, V. Gupta, Applied Physics Letters, 2016, 108, 211603.

[24] X.K. Ning, Z.J. Wang, Y.N. Chen, Z.D. Zhang, Nanoscale, **2015**, 7, 20635-20641.

[25] J.H. Cho, Q.X. Jia, X.D. Wu, S.R. Foltyn, M.P. Maley, Physical Review B, **1996**, 54, 37-40.

[26] G.P. Mambrini, E.R. Leite, M.T. Escote, A.J. Chiquito, E. Longo, J.A. Varela, R.F. Jardim, Journal of Applied Physics, **2007**, 102, 043708.

[27] M. Zhu, P. Komissinskiy, A. Radetinac, Z. Wang, L. Alff, Journal of Applied Physics, **2015**, 117 , 155306.

[28] Y.J. Chang, C.H. Kim, S.H. Phark, Y.S. Kim, J. Yu, T.W. Noh, Physical review letters, **2009**, 103, 057201.

[29] D.S.L. Pontes, F.M. Pontes, M.A. Pereira-da-Silva, O.M. Berengue, A.J. Chiquito, E. Longo, Ceramics International, **2013**, 39, 8025-8034.

[30] N. Gayathri, A.K. Raychaudhuri, X.Q. Xu, J.L. Peng, R.L. Greene, Journal of Physics: Condensed Matter,**1998**, 10, 1323-1338.

[31] P.J. Ford, J.A. Mydosh, Physical Review B, **1976**, 14, 2057-2070.

[32] O. Morán, W. Saldarriaga, E. Baca, Superlattices and Microstructures, **2013**, 55, 151-160.

[33] B. Pang, L. Zhang, Y.B. Chen, J. Zhou, S. Yao, S. Zhang, Y. Chen, Applications, ACS applied materials & interfaces, **2017**, 9, 3201-3207.
[34] R. Palai, H. Huhtinen, J.F. Scott, R.S. Katiyar, Physical Review B, **2009**, 79, 104413.
[35] M. Zheng, X. Li, W. Xiao, W. Wang, H. Ni, Applied Physics Letters, **2017**, 111, 152405.
[36] X.K. Ning, Z.J. Wang, Z.D. Zhang, Journal of Applied Physics, **2015**, 117, 093907.
[37] S. Lin, Q. Zhang, M.A. Roldan, S. Das, T. Charlton, M.R. Fitzsimmons, Q. Jin, S. Li, Z. Wu, S. Chen, H. Guo, X. Tong, M. He, C. Ge, C. Wang, L. Gu, K.-j. Jin, E.-J. Guo, Physical Review Applied, **2020**, 13, 034033.

[38] L.M. Wang, H.E. Horng, H.C. Yang, Physical Review B, **2004**, 70, 014433.
[39] P. Kaur, K.K. Sharma, R. Pandit, R.J. Choudhary, R. Kumar, Applied Physics Letters, **2014**, 104, 081608.
[40] C. Sow, D. Samal, P.S.A. Kumar, A.K. Bera, S.M. Yusuf, Physical Review B, **2012**, 85, 224426.
[41] Y. Jean, C.T. Marsden, Molecular Orbitals of Transition Metal Complexes, OUP Oxford, **2005**.
[42] S. Catalano, M. Gibert, J. Fowlie, J. Iniguez, J.M. Triscone, J. Kreisel, Physical Society, **2018**, 81, 046501.
[43] P. Liu, X. Ning, Materials Research Letters, **2020**, 8, 173-179.